RSC Advances

PAPER

View Article Online
View Journal | View Issue

Cite this: *RSC Adv.*, 2026, **16**, 16944

High-sensitivity optical thermometry in Tb^{3+}/Eu^{3+} co-doped $Li_2Y_4(MoO_4)_7$ phosphors synthesized *via* solid-state reaction

Fadwa Ayachi,[a] Kamel Saidi,[ab] Mohamed Dammak,*[a] I. Mediavilla-Martínez[c] and J. Jimenez[c]

Received 23rd February 2026
Accepted 24th March 2026

DOI: 10.1039/d6ra01596d

rsc.li/rsc-advances

Developing ratiometric optical thermometers with high sensitivity and signal stability remains a critical challenge in non-contact temperature sensing. Herein, a series of 5% Eu^{3+}, 40% Tb^{3+} doped, and 40% Tb^{3+}/5% Eu^{3+} co-doped $Li_2Y_4(MoO_4)_7$ (LiYMoO:Tb/Eu) phosphors were synthesized utilizing a conventional solid-state reaction route. Structural refinement and morphological inspections confirmed the phase purity and crystallinity of the resulting molybdate host. Under 325 nm ultraviolet excitation, the photoluminescence spectra revealed a multi-center emission profile, featuring characteristic transitions of Tb^{3+} (green) and Eu^{3+} (red) host framework, indicating an efficient energy transfer network among the dopants and the host. To evaluate the material's potential for thermometry, the fluorescence intensity ratio (FIR) technique was applied using the non-thermally coupled transitions of Tb^{3+} ($^5D_4 \rightarrow {}^7F_5$ at 542 nm) and Eu^{3+} ($^5D_0 \rightarrow {}^7F_4$ at 701 nm). The thermometric performance was investigated over the physiological and industrial temperature range of 300–403 K. Notably, the phosphor exhibited a superior maximum relative sensitivity (S_r) of 6.5% K^{-1} at 300 K, significantly outperforming many existing molybdate-based sensors. These findings suggest that the 40% Tb^{3+}/5% Eu^{3+} co-doped $Li_2Y_4(MoO_4)_7$ system is a promising candidate for precise optical temperature sensing applications.

1. Introduction

In recent years, lanthanide-doped luminescent materials have attracted significant scientific interest due to their multifunctional capabilities in next-generation solid-state lighting (SSL), optical display technologies, and non-contact temperature sensing.[1–6] The development of high-performance phosphors requires a careful selection of the host matrix, as its crystal field environment and phonon energy critically influence the radiative and non-radiative relaxation pathways of the dopant ions. Among the various oxide hosts, molybdate compounds have emerged as exceptional candidates owing to their high chemical stability, excellent thermal durability, and moderate phonon energy, which minimizes quenching losses.[7,8]

A strategic approach to optimizing luminescent performance involves the co-doping of rare-earth (RE^{3+}) ions to exploit energy transfer (ET) mechanisms. Europium (Eu^{3+}) is widely recognized as a superior activator for red emission, characterized by its intense $^5D_0$ to $^7F_2$ transition, which is essential for improving the color rendering index (CRI) and warm-light components in white light-emitting diodes (W-LEDs).[9,10] Conversely, terbium (Tb^{3+}) provides a distinct green emission *via* the $^5D_4$ to $^7F_5$ transition at approximately 542 nm. While singly doped materials are limited to monochromatic outputs, the Tb^{3+}/Eu^{3+} co-doped system has garnered considerable attention because it enables color tunability through efficient Tb^{3+} to Eu^{3+} energy transfer. This mechanism allows for the precise adjustment of emission chromaticity from green to red by modulating dopant concentrations, offering a versatile platform for tunable LED components.[11,12] Beyond illumination, these RE^{3+}-doped phosphors are increasingly utilized for optical thermometry, a technique that overcomes the limitations of conventional contact sensors in harsh or electromagnetic environments. The Fluorescence Intensity Ratio (FIR) method, which relies on the intensity ratio of two distinct emission bands, is particularly favored for its immunity to fluctuations in excitation power and spectrum losses.[13] Building upon our previous investigations into rare-earth-doped phosphors, our group has extensively explored the thermometric potential of various host matrices. We have previously demonstrated high-sensitivity sensing in systems such as Er^{3+}/Yb^{3+} co-doped molybdates and vanadates, where energy transfer plays

[a]*Laboratoire de Physique Appliquée, Faculté des Sciences de Sfax, Département de Physique, Université de Sfax, BP 1171, Sfax, Tunisia. E-mail: mohamed.dammak@fss.usf.tn; madidammak@yahoo.fr*

[b]*Department of Physics, Sfax Preparatory Engineering Institute, University of Sfax, 1172-3000, Sfax, Tunisia*

[c]*GdS Optronlab, Department of Condensed Matter Physics, LUCIA Building University of Valladolid, Paseo de Belen 19, 47011, Valladolid, Spain*

a pivotal role in signal stability.[14,15] For instance, our recent work on $Na_3Y(VO_4)_2$:Eu^{3+} highlighted the efficacy of Eu^{3+} transitions for temperature monitoring,[16] while our studies on phosphate matrices elucidated the mechanisms of color tuning *via* Tb^{3+}/Eu^{3+} interaction.[17] However, the exploration of the $Li_2Y_4(MoO_4)_7$ host remains limited.

The present work does not aim to provide a comprehensive study of energy transfer dynamics between Tb^{3+} and Eu^{3+} ions, but rather to exploit the thermally distinct emission responses of their characteristic bands as the basis for high-sensitivity non-contact LIR thermometry in the novel $Li_2Y_4(MoO_4)_7$ host.

In this study, we report the synthesis of a novel series of Tb^{3+}, Eu^{3+}, and Tb^{3+}/Eu^{3+} co-doped $Li_2Y_4(MoO_4)_7$ (LiYMoO) phosphors *via* a conventional solid-state reaction. We present a systematic analysis of their structural phase purity and morphological characteristics. Furthermore, we investigate the photoluminescence properties and the Tb^{3+} to Eu^{3+} energy transfer mechanism in detail. A key focus of this work is to evaluate the optical thermometry performance of the co-doped system using the FIR technique under 325 nm excitation. The results are compared with our previous findings to demonstrate the superior relative sensitivity and signal reproducibility of the $Li_2Y_4(MoO_4)_7$ matrix, establishing its suitability for sensing applications.

2. Experimental section

2.1. Sample synthesis

A series of LiYMoO phosphors, including singly doped (Eu^{3+}, Tb^{3+}) and co-doped (Tb^{3+}/Eu^{3+}) samples, were synthesized *via* a conventional high-temperature solid-state reaction method. The starting precursors employed were analytical grade lithium carbonate (Li_2CO_3, 99.99%), molybdenum trioxide (MoO_3, 99.99%), yttrium oxide (Y_2O_3, 99.99%), terbium oxide (Tb_4O_7, 99.99%), and europium oxide (Eu_2O_3, 99.99%). Stoichiometric amounts of the raw materials were accurately weighed according to the nominal composition of $Li_2Y_{\{4-x-y\}}Tb_xEu_y(MoO_4)_7$. The powders were thoroughly ground in an agate mortar with a small quantity of ethanol to facilitate homogenization. After drying, the mixtures were transferred into alumina crucibles and sintered in an electric furnace at 1273 K for 8 h in an air atmosphere. Finally, the obtained products were naturally cooled to room temperature and ground into fine powders for further characterization.

2.2. Characterization techniques

The phase purity and crystal structure of the as-prepared phosphors were identified by X-ray diffraction (XRD) using a Bruker AXS D8 diffractometer equipped with Cu K alpha radiation (lambda = 1.5406 Å). The surface morphology and particle size distribution were examined using a field-emission scanning electron microscope (FE-SEM, Hitachi SU-4800). Photoluminescence (PL) measurements were conducted at room temperature using a high-resolution Horiba-Jobin Yvon LabRAM HR 800 UV Raman spectrometer coupled with an Olympus BX41 confocal microscope. The excitation source was the 325 nm line of a He–Cd continuous-wave laser. The emitted signal was detected by a charge-coupled device (CCD) detector. Spectral resolution was controlled using holographic gratings with groove densities of 2400 lines per mm (for high-resolution scans) and 150 lines per mm (for broad surveys) and the spectral resolution was approximately ~1 nm. To prevent thermal heating effects during measurement, the laser power incident on the sample surface was maintained below 1 mW, corresponding to an irradiance of less than 100 kW cm^{-2}, for which no line shifts were observed.

3. Results and discussion

3.1. Structural analysis and phase purity

The phase composition and crystal structure of the synthesized LiYMoO phosphors singly doped with 5% Eu^{3+} and 40% Tb^{3+}, as well as co-doped with ion patterns are presented in Fig. 1. The detected diffraction peaks are in accordance well with the standard $Na_{0.5}Gd_{0.5}MoO_4$ (JCPDS 25-0829) which is of a single phase with tetragonal scheelite structure and a space group $I4_1/a$. The diffraction data are consistent with the general family of defect scheelite-type double molybdates with composition $A_2Ln_4(MoO_4)_7$ (where A = alkali metal, Ln = rare-earth element). No secondary phases or impurity peaks related to unreacted precursors were detected, confirming that the synthesis conditions (1273 K for 8 h) were sufficient to obtain a pure, single-phase solid solution. The sharp and intense diffraction peaks attest to the high crystallinity of the samples. Furthermore, the incorporation of Eu^{3+} and Tb^{3+} activators into the host lattice did not induce any significant shift in peak positions or observable changes in the diffraction profiles. This structural stability is attributed to the successful isovalent substitution of

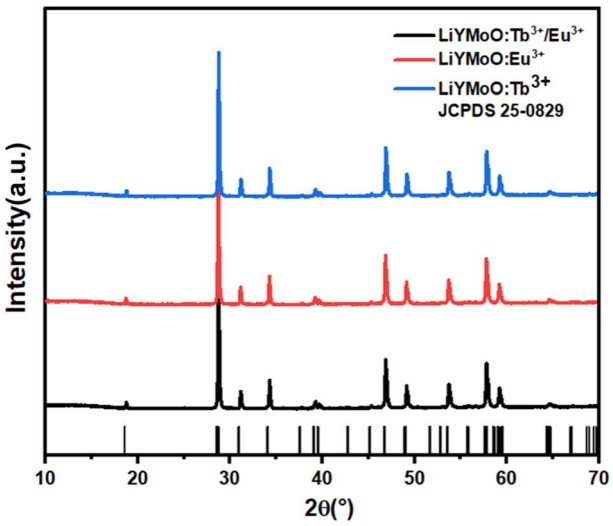

Fig. 1 XRD patterns of $Li_2Y_4(MoO_4)_7$:Tb^{3+} (40 mol%), $Li_2Y_4(MoO_4)_7$:-Eu^{3+} (5 mol%), and co-doped $Li_2Y_4(MoO_4)_7$:Tb^{3+} (40 mol%)/Eu^{3+} (5 mol%) phosphors synthesized by solid-state reaction, together with the standard JCPDS reference pattern for the $Li_2Y_4(MoO_4)_7$ tetragonal scheelite-type structure. The absence of secondary phase reflections confirms the phase purity of all compositions.

Y^{3+} ions by Eu^{3+} and Tb^{3+} ions at the same crystallographic site, which is facilitated by the close similarity of their ionic radii. According to Shannon's crystal ionic radii tables,[18] all three ions share coordination number CN = 8 with the following values: Y^{3+} (1.019 Å), Tb^{3+} (1.040 Å), and Eu^{3+} (1.066 Å), corresponding to lattice mismatch values of only +2.1% and +4.6% for Tb^{3+} and Eu^{3+} with respect to Y^{3+}, respectively. These marginal size differences are well within the tolerance range for solid-solution substitution without structural distortion. Consequently, the structural integrity of the $Li_2Y_4(MoO_4)_7$ host matrix is fully preserved across all doping compositions, as evidenced by the absence of systematic lattice parameter shifts and the conservation of the tetragonal scheelite-type structure throughout the entire series.

To further confirm the phase purity and crystal structure of the synthesized LiYMoO:Tb^{3+}, LiYMoO:Eu^{3+} and LiYMoO:5% Eu^{3+}/40% Tb^{3+} phosphors, Rietveld refinement of the powder XRD data were performed using the tetragonal scheelite-type structural model with space group $I4_1/a$. The refined patterns are presented in Fig. 2. Rietveld refinement of the XRD patterns confirmed that both Tb^{3+}, Eu^{3+} and Eu^{3+}/Tb^{3+} doped LiYMoO phosphors crystallize in the tetragonal scheelite-type structure (space group $I4_1/a$) without secondary phases. The good agreement between experimental and calculated patterns indicates high crystallinity and phase purity. Eu^{3+}, Tb^{3+} and Eu^{3+}/Tb^{3+} ions enter into Y^{3+} sites without inducing structural distortion, thereby preserving the structural stability of the host lattice. Table 1 lists the crystals cell and structural properties.

3.2. Morphological characterization

The surface morphology and particle microstructure were examined by Scanning Electron Microscopy (SEM). Fig. 3 displays representative SEM micrographs of the undoped, singly doped, and co-doped LiYMoO samples.

The micrographs reveal that the samples consist of agglomerated particles with irregular shapes and distinct boundaries, a characteristic feature of ceramic phosphors prepared *via* the high-temperature solid-state reaction route. The particle sizes generally range from 3 to 10 μm. Comparative analysis of the images indicates that the introduction of Eu^{3+} and Tb^{3+} dopants had no significant impact on the overall morphology or grain size distribution. The microstructure remains uniform across all compositions, suggesting that the doping concentration does not alter the grain growth kinetics during the sintering process. This micron-scale particle size is favorable for phosphor applications, as it typically enables easier coating and better light extraction efficiency in packaged devices.

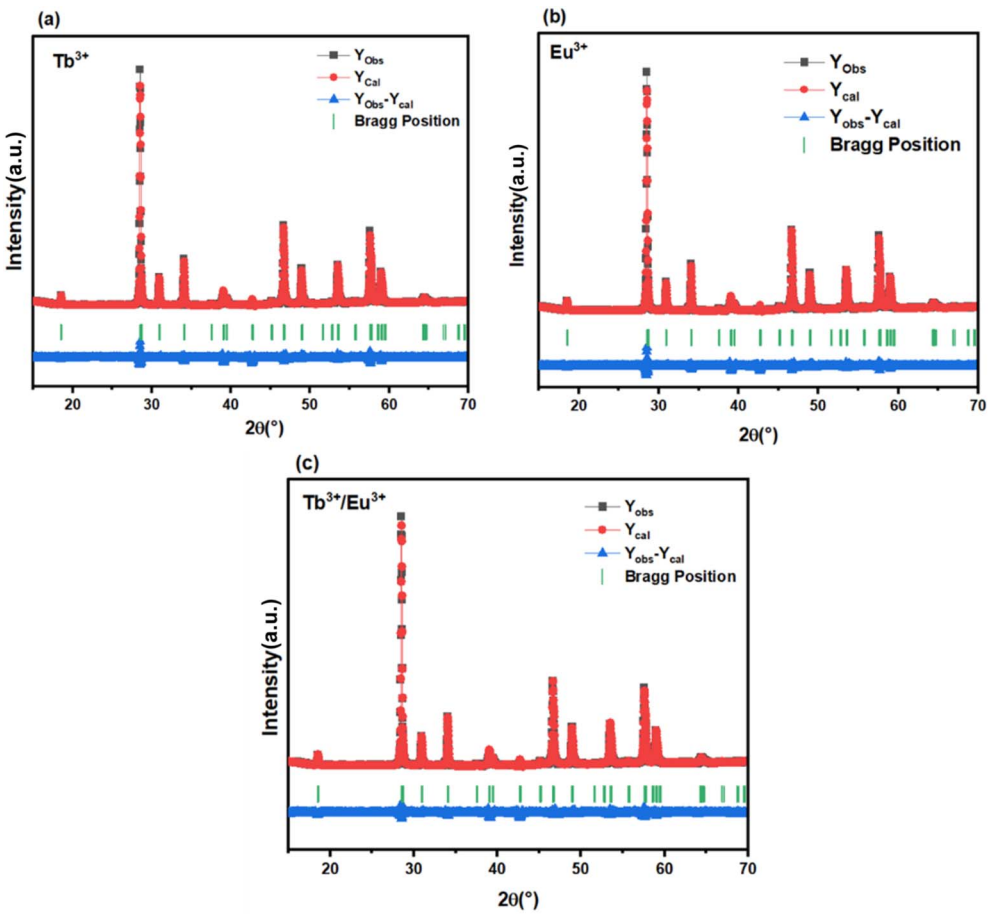

Fig. 2 Refined powder X-ray diffraction pattern for $Li_2Y_4(MoO_4)_7$ samples (a) 40% Tb^{3+}, (b) 5% Eu^{3+} and (c) 40% Tb^{3+}/5% Eu^{3+}.

Table 1 Rietveld refinement parameters from XRD analysis

Sample	$\alpha = \beta = \gamma$	a (Å)	b (Å)	c (Å)	V (Å^3)	R_{wp} (%)	χ^2
$Li_2Y_4(MoO_4)_7$:40% Tb^{3+}	90°	5.26361	5.26361	11.56449	320.400	6.60	2.2
$Li_2Y_4(MoO_4)_7$:5% Eu^{3+}	90°	5.26353	5.26353	11.56436	320.387	5.00	2.4
$Li_2Y_4(MoO_4)_7$:40% Tb^{3+}/5% Eu^{3+}	90°	5.26361	5.26361	11.56458	320.404	9.4	2.1

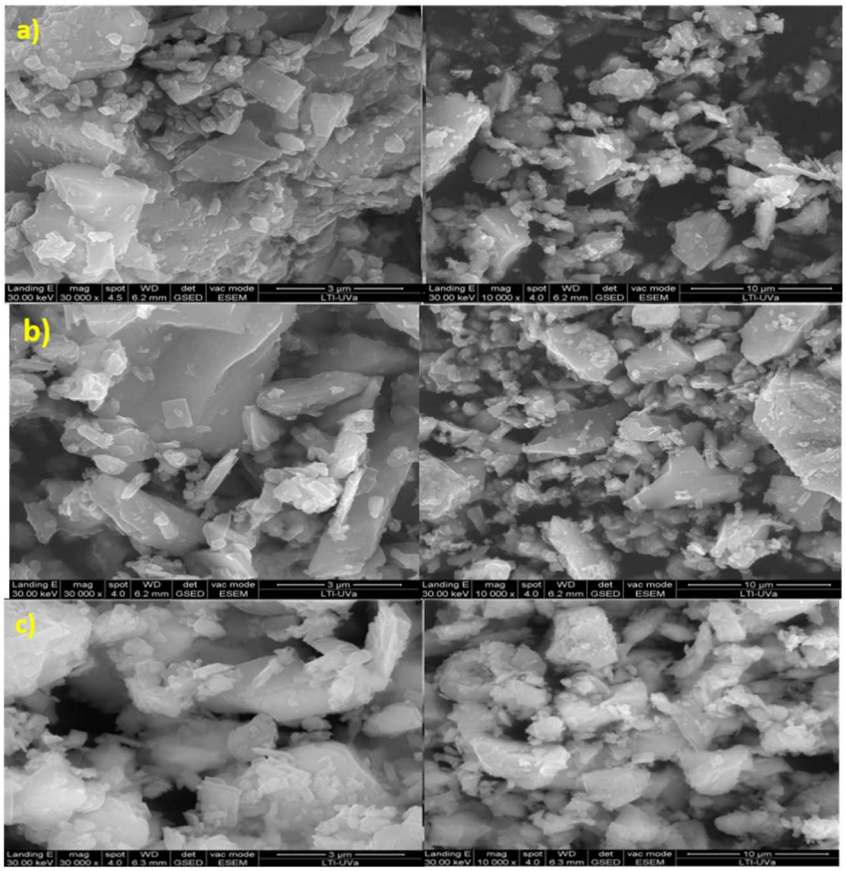

Fig. 3 SEM images of the (a) LiYMoO:40% Tb^{3+}, (b) LiYMoO:5% Eu^{3+} and (c) LiYMoO:40% Tb^{3+}/5% Eu^{3+}.

4. Luminescence properties

4.1. Photoluminescence properties and spectral analysis

The room-temperature photoluminescence (PL) spectra of the LiYMoO phosphors doped with Tb^3, Eu^{3+}, and codoped with Tb^{3+}/Eu^{3+} under near-UV excitation (325 nm) are plotted in Fig. 4(a). The excitation at 325 nm is well-suited for this system for two complementary reasons: (i) it falls within the charge-transfer absorption band of the $[MoO_4]^{2-}$ polyanionic groups, which act as sensitizers that transfer energy to both Tb^{3+} and Eu^{3+} ions; and (ii) it overlaps with 4f–4f absorption transitions of both lanthanide ions, enabling their direct excitation.[23]

The spectrum of the Tb^{3+} doped sample exhibits a series of sharp emission bands characteristic of the $^5D_4$ to $^7F_{J\ (J=6,5,4,3)}$ transitions. The peaks centered at 488, 542, 585, and 621 nm are ascribed to the $^5D_4 \rightarrow {}^7F_6$, $^5D_4 \rightarrow {}^7F_5$, $^5D_4 \rightarrow {}^7F_4$, and $^5D_4 \rightarrow {}^7F_3$ transitions, respectively. Among these, the green emission at 542 nm ($^5D_4 \rightarrow {}^7F_5$) is the most dominant. The Eu^{3+} doped sample displays a distinct spectral profile featuring multiple narrow peaks arising from the intra-configurational 4f–4f transitions of Eu^{3+}. These are identified as the $^5D_0 \rightarrow {}^7F_0$ (578 nm), $^5D_0 \rightarrow {}^7F_1$ (592 nm), $^5D_0 \rightarrow {}^7F_2$ (612 nm), $^5D_0 \rightarrow {}^7F_3$ (653 nm), and $^5D_0 \rightarrow {}^7F_4$ (701 nm) transitions. The hypersensitive electric dipole transition ($^5D_0 \rightarrow {}^7F_2$) at 612 nm exhibits the highest intensity, resulting in a strong red emission for the Tb^{3+}/Eu^{3+} co-doped sample, the PL spectrum reveals a dual-emission character, containing the characteristic peaks of both Tb^{3+} (green) and Eu^{3+} (red) ions, notably, the simultaneous presence of these bands under an excitation wavelength that primarily targets the host and Tb^{3+} levels suggest the existence of an efficient energy transfer pathway within the matrix.

4.2. Energy transfer mechanism

Under typical conditions, Tb^{3+} ions can act as sensitizers for Eu^{3+} ions, enhancing the Tb^{3+} emission. In this study, the

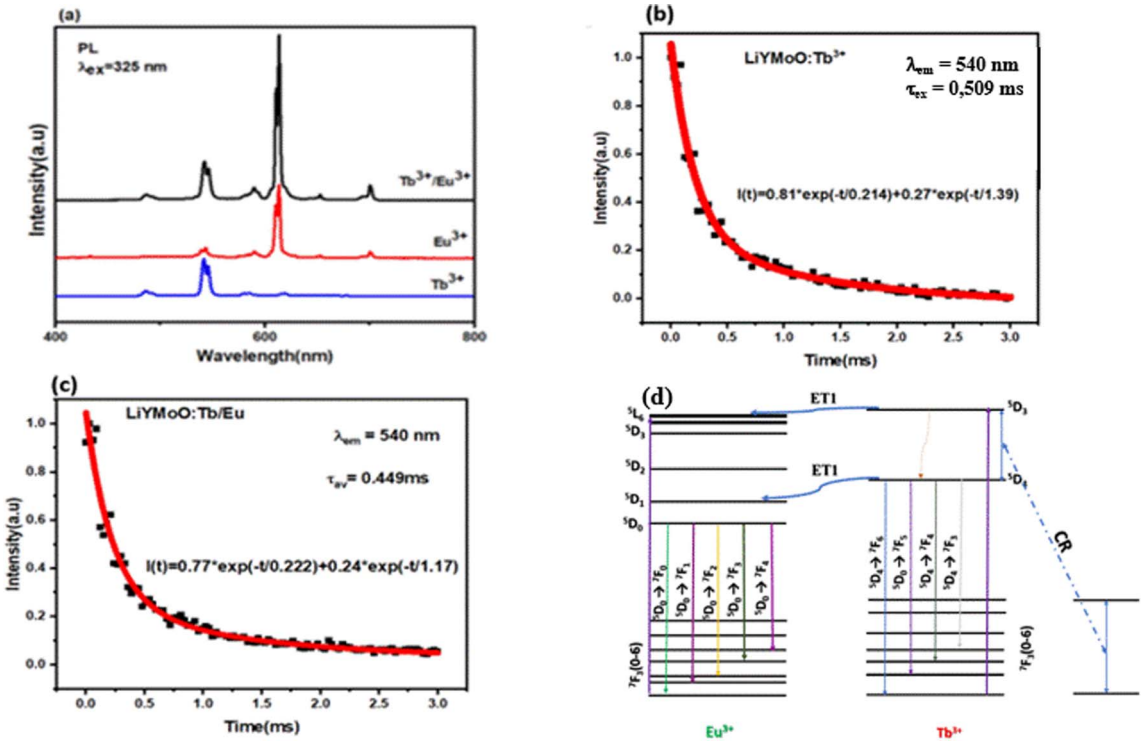

Fig. 4 (a) Photoluminescence (PL) emission spectra under 325 nm excitation of singly doped $Li_2Y_4(MoO_4)_7$:Tb^{3+} (40 mol%), singly doped $Li_2Y_4(MoO_4)_7$:Eu^{3+} (5 mol%), and co-doped $Li_2Y_4(MoO_4)_7$:Tb^{3+} (40 mol%)/Eu^{3+} (5 mol%) phosphors, illustrating the characteristic Tb^{3+} ($^5D_4 \rightarrow {}^7F_J$) and Eu^{3+} ($^5D_0 \rightarrow {}^7F_J$) emission bands and the effect of co-doping on their relative intensities. (b) Luminescence decay curve of the Tb^{3+} $^5D_4$ emission (540 nm) in the singly doped $Li_2Y_4(MoO_4)_7$:Tb^{3+} (40 mol%) phosphor under 325 nm excitation. (c) Luminescence decay curve of the Tb^{3+} $^5D_4$ emission (540 nm) in the co-doped $Li_2Y_4(MoO_4)_7$:Tb^{3+} (40 mol%)/Eu^{3+} (5 mol%) phosphor, showing the reduction in donor lifetime due to $Tb^{3+} \rightarrow Eu^{3+}$ energy transfer with an efficiency of $\eta_{ET} \approx 12\%$. (d) Schematic energy level diagram of Tb^{3+} and Eu^{3+} ions illustrating the excitation pathways, radiative transitions, and non-radiative $Tb^{3+} \rightarrow Eu^{3+}$ energy transfer process under 325 nm excitation.

doping concentrations of Tb^{3+} and Eu^{3+} ions were fixed at 40% and 5%, respectively.

Therefore, to carefully estimate the ET efficiency (η_{ET}) from Tb^{3+} to Eu^{3+} ions we measured the lifetimes of Tb^{3+} ion and Tb^{3+}/Eu^{3+} as illustrated in Fig. 4(b) and (c), respectively and this can be expressed by the equation of Paulose:[19,20]

$$\eta_{ET} = 1 - \frac{\tau}{\tau_0} \quad (1)$$

Here, τ and τ_0 are the lifetimes of the sensitizer Tb^{3+} in the presence and absence of the activator Eu^{3+} ions, respectively. The energy transfer efficiency value is about 12%, which suggests that the energy transfer from Tb^{3+} to Eu^{3+} is performing efficiently.

To elucidate the interaction between the dopants, the energy transfer (ET) mechanism in the Tb^{3+}/Eu^{3+} co-doped system is schematically illustrated in Fig. 4(d). The mechanism relies on Tb^{3+} acting as an effective sensitizer for Eu^{3+}. Upon excitation at 325 nm, Tb^{3+} ions are promoted to high-energy excited states and subsequently relax non-radiatively to the metastable $^5D_4$ level. While a portion of this energy is released radiatively (green emission), a significant fraction is transferred non-radiatively to the neighboring Eu^{3+} ions *via* phonon-assisted energy transfer. This process is facilitated by the spectral overlap between the emission energy of the Tb^{3+} donor ($^5D_4 \rightarrow {}^7F_{\{6,5\}}$) and the absorption energy levels of the Eu^{3+} acceptor. Consequently, the Eu^{3+} ions are excited to the $^5D_0$ state and decay radiatively to the ground state manifold (^7F_J), intensifying the red emission ($^5D_0 \rightarrow {}^7F_2$). This synergistic interaction not only enhances the overall luminescence efficiency, but also enables the tuning of the emission color by modulating the Tb/Eu ratio.

4.3. Chromaticity coordinates (CIE)

The influence of co-doping on the perceived emission color was quantified using Commission Internationale de l'Éclairage (CIE 1931) chromaticity coordinates, as depicted in Fig. 5.

The chromaticity analysis reveals a clear evolution of the emission color depending on the dopant composition. In the Tb^{3+}-doped sample, the coordinates are located in the deep green region of the CIE diagram, which is consistent with the dominant $^5D_4 \rightarrow {}^7F_5$ transition centered at 542 nm. In contrast, the Eu^{3+}-doped sample exhibits chromaticity coordinates situated in the reddish-orange region, mainly driven by the intense $^5D_0 \rightarrow {}^7F_2$ electric-dipole transition at 612 nm. For the Tb^{3+}/Eu^{3+} codoped sample, the chromaticity coordinates shift toward the orange to warm-white region. This shift represents the macroscopic manifestation of the microscopic energy transfer mechanism between Tb^{3+} and Eu^{3+} ions, where the effective mixing of the green emission from Tb^{3+} and the red emission from Eu^{3+} results in a tunable orange luminescence. By adjusting the $[Tb^{3+}]/[Eu^{3+}]$ ratio, the emission color can be precisely controlled.

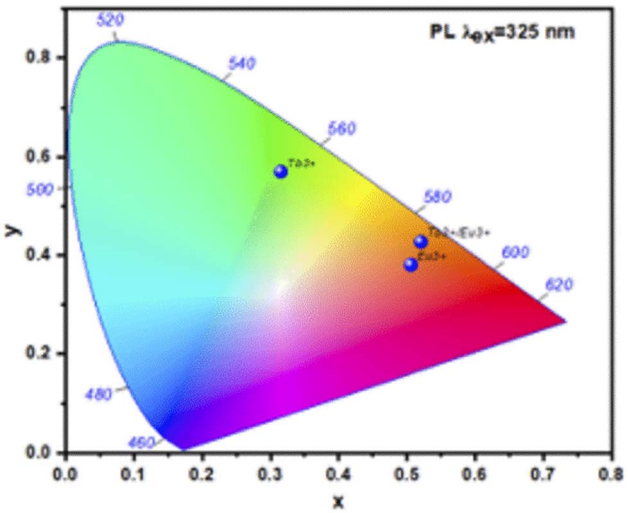

Fig. 5 Commission Internationale de l'Éclairage (CIE) 1931 chromaticity diagram showing the color coordinates of the singly doped $Li_2Y_4(MoO_4)_7$:Tb^{3+} (40 mol%), singly doped $Li_2Y_4(MoO_4)_7$:Eu^{3+} (5 mol%), and co-doped $Li_2Y_4(MoO_4)_7$:Tb^{3+} (40 mol%)/Eu^{3+} (5 mol%) phosphors under 325 nm excitation, demonstrating the color tunability from green (Tb^{3+}-dominated) to orange-red (Eu^{3+}-dominated) emission achievable through lanthanide co-doping in the $Li_2Y_4(MoO_4)_7$ host matrix.

5. Temperature-dependent luminescence and optical thermometry

To assess the potential of the synthesized material for contactless temperature sensing, the photoluminescence properties of the Tb^{3+}/Eu^{3+} co-doped LiYMoO phosphor were systematically investigated under 325 nm excitation over the temperature range of 300–403 K. The temperature-dependent PL spectra are illustrated in Fig. 6.

The Eu^{3+} emission ($^5D_0 \rightarrow {}^7F_2$, 615 nm) undergoes progressive thermal quenching with increasing temperature, while the Tb^{3+} emission ($^5D_4 \rightarrow {}^7F_5$, 545 nm) exhibits a thermally activated enhancement in the range 300–403 K. This asymmetric and opposite thermal behavior of the two emission centers constitutes the physical basis enabling high-sensitivity LIR thermometry in this system, as it maximizes the rate of change of the intensity ratio with temperature.

The temperature-dependent luminescence behavior of the Tb^{3+}/Eu^{3+} co-doped $Li_2Y_4(MoO_4)_7$ phosphor reveals an asymmetric thermal response between the two emitting centers. While the Eu^{3+} emission ($^5D_0 \rightarrow {}^7F_2$, 612 nm) undergoes progressive thermal quenching with increasing temperature consistent with thermally activated non-radiative relaxation *via* the host lattice phonons: the Tb^{3+} emission ($^5D_4 \rightarrow {}^7F_5$, 542 nm) exhibits a thermally activated enhancement in the range 300–403 K. This behavior arises from the interplay of three physical mechanisms: (i) thermally enhanced multi-phonon relaxation from the higher-lying $^5D_3$ level of Tb^{3+} to the emitting $^5D_4$ level, which increases $^5D_4$ population at elevated temperatures; (ii)

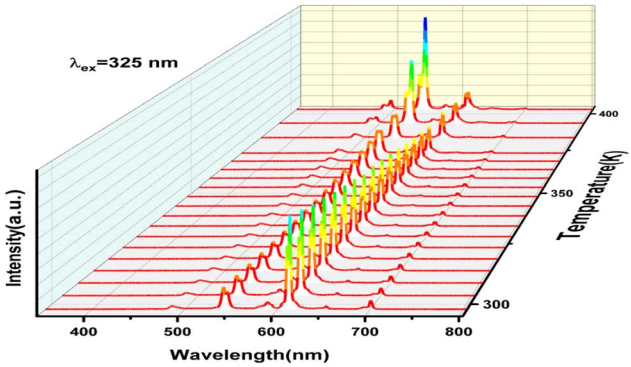

Fig. 6 Temperature-dependent photoluminescence (PL) emission spectra of the co-doped $Li_2Y_4(MoO_4)_7$:Tb^{3+} (40 mol%)/Eu^{3+} (5 mol%) phosphor under 325 nm (He–Cd laser) excitation, recorded over the temperature range 300–403 K, showing the simultaneous spectral evolution of the Tb^{3+} ($^5D_4 \rightarrow {}^7F_J$, 480–630 nm) and Eu^{3+} ($^5D_0 \rightarrow {}^7F_J$, 578–720 nm) emission bands with increasing temperature.

a temperature-dependent reduction in the $Tb^{3+} \rightarrow Eu^{3+}$ non-radiative energy transfer efficiency, which decreases with rising temperature due to the increased phonon-assisted back-transfer probability, thereby retaining more excitation energy in the Tb^{3+} $^5D_4$ level; and (iii) the lower activation energy for non-radiative decay of Eu^{3+} relative to Tb^{3+} in the molybdate host, causing preferential quenching of Eu^{3+} emission. Taken together, these effects produce the observed asymmetric thermal behavior, where the Eu^{3+} emission weakens while the Tb^{3+} emission is temporarily enhanced, maximizing the rate of change of the LIR with temperature and thereby providing the physical basis for the high thermometric sensitivity of this system.

The diverse thermal response of the two emission centers (Tb^{3+} and Eu^{3+}) allows for the application of the Fluorescence Intensity Ratio (FIR). This method mitigates measurement errors arising from fluctuations in excitation power or sample geometry. To identify the optimal thermometric signal, four distinct FIR modes were defined based on the ratio of integrated intensities of the non-thermally coupled levels of Tb^{3+} and Eu^{3+}: $FIR_1 = I_{485}/I_{612}$, $FIR_2 = I_{485}/I_{701}$, $FIR_3 = I_{542}/I_{612}$, $FIR_4 = I_{542}/I_{701}$.

As shown in Fig. 7, all calculated FIR values exhibit a monotonic and non-linear evolution with temperature from 300 to 403 K.

To quantify this behavior, the experimental data for all FIR modes were fitted using a cubic polynomial function, given by:[21,22]

$$FIR = A + B \times T + C \times T^2 + D \times T^3 \quad (2)$$

where T is the absolute temperature, and A, B, C, and D are the fitting coefficients (Table 2).

The performance of an optical thermometer is critically evaluated using two figures of merit: absolute sensitivity (S_a) and relative sensitivity (S_r). These parameters are defined as:[23–25]

$$S_a = \frac{dFIR}{dT} = 3DT^2 + 2CT + B \quad (3)$$

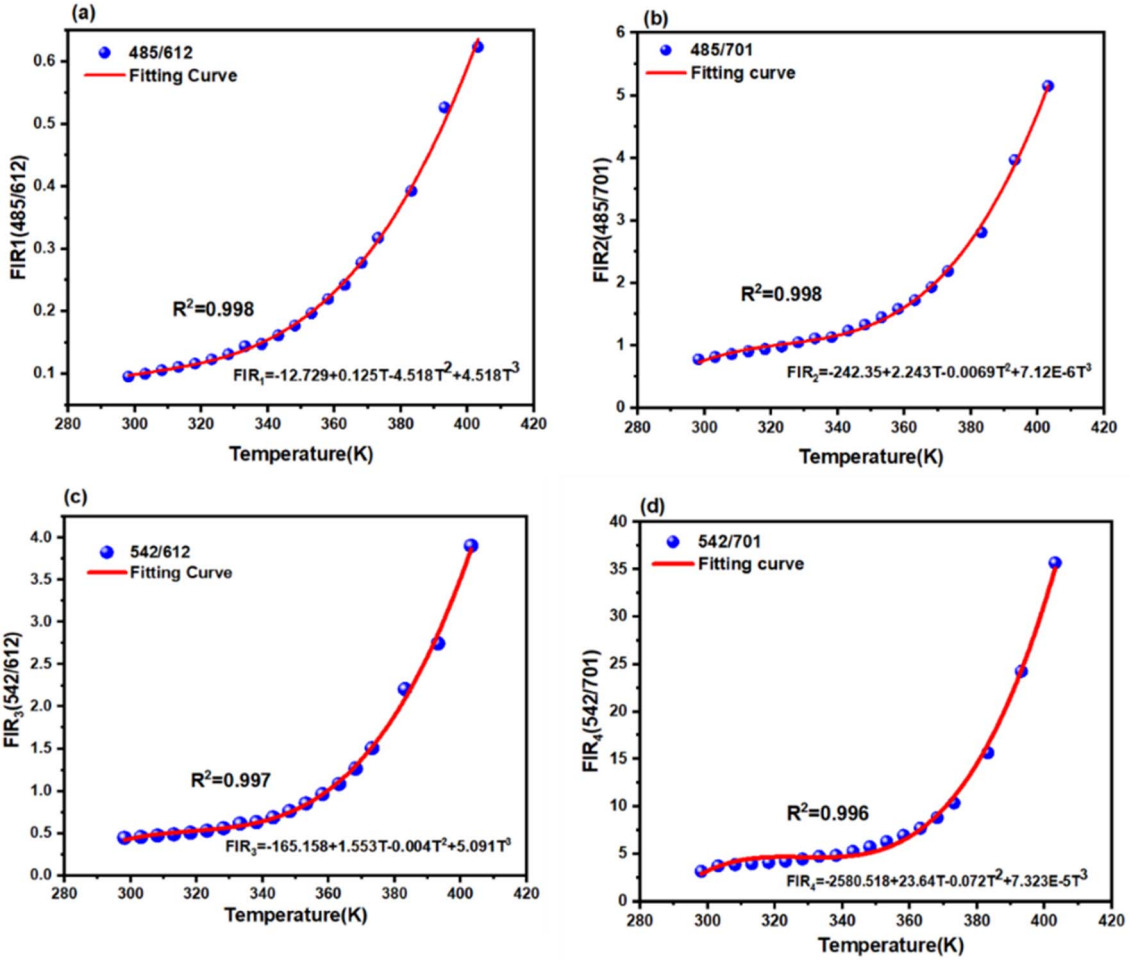

Fig. 7 Temperature dependence of the fluorescence intensity ratio (FIR/LIR) for the co-doped $Li_2Y_4(MoO_4)_7$:Tb^{3+} (40 mol%)/Eu^{3+} (5 mol%) phosphor under 325 nm excitation, constructed from four independent emission band combinations: (a) I_{485}/I_{612}, corresponding to the Tb^{3+} $^5D_4$ → $^7F_3$ (485 nm) and Eu^{3+} $^5D_0$ → $^7F_2$ (612 nm) transitions; (b) I_{485}/I_{701}, corresponding to the Tb^{3+} $^5D_4$ → $^7F_3$ (485 nm) and Eu^{3+} $^5D_0$ → $^7F_4$ (701 nm) transitions; (c) I_{542}/I_{612}, corresponding to the Tb^{3+} $^5D_4$ → $^7F_5$ (542 nm) and Eu^{3+} $^5D_0$ → $^7F_2$ (612 nm) transitions; and (d) I_{542}/I_{701}, corresponding to the Tb^{3+} $^5D_4$ → $^7F_5$ (542 nm) and Eu^{3+} $^5D_0$ → $^7F_4$ (701 nm) transitions, in the temperature range 300–403 K.

$$S_r = \frac{1}{\mathrm{FIR}} \frac{\delta \mathrm{FIR}}{\delta T} = \frac{1}{\mathrm{FIR}} \times 3DT^2 + 2CT + B. \quad (4)$$

Fig. 8 depicts the temperature dependence of S_a and S_r for the investigated FIR modes. Among the four studied ratios, the $FIR_4(I_{542}/I_{701})$ mode demonstrates the superior performance. It achieves a maximum absolute sensitivity (S_a) of 1.22 K^{-1} at 403 K and a remarkable relative sensitivity (S_r) of 6.5% K^{-1} at 300 K. This high relative sensitivity value significantly surpasses that of many previously reported rare-earth doped molybdate phosphors,[26] positioning the Tb^{3+}/Eu^{3+} co-doped LiYMoO system as a highly competitive candidate for high-precision optical thermometry in the physiological and industrial temperature ranges.

To properly evaluate the thermometric performance of the synthesized phosphors, a comparative analysis was conducted against other recently reported Tb^{3+}/Eu^{3+} co-doped hosts. Table

Table 2 Transitions used for the different intensity ratio techniques, wavelengths, fitted equations, correlation coefficients and maxima values for the relative sensitivity

Transitions	λ (nm)	Equation	S_r (max) (% K^{-1})
Tb^{3+}:$^5D_4$ → $^7F_6$, Eu^{3+}:$^5D_0$ → $^7F_2$	485/612	$-12.729 + 0.125T - 4.518T^2 + 4.518T^3$	2.5 (400 K)
Tb^{3+}:$^5D_4$ → $^7F_6$, Eu^{3+}:$^5D_0$ → $^7F_4$	485/701	$-242.35 + 2.243T - 0.0069T^2 + 7.12 \times 10^{-6}T^3$	2.7 (300 K), 3 (400 K)
Tb^{3+}:$^5D_4$ → $^7F_5$, Eu^{3+}:$^5D_0$ → $^7F_2$	542/612	$-165.158 + 1.553T - 0.004T^2 + 5.091T^3$	3.4 (400 K)
Tb^{3+}:$^5D_4$ → $^7F_5$, Eu^{3+}:$^5D_0$ → $^7F_4$	542/701	$-2580.518 + 23.64T - 0.072T^2 + 7.323 \times 10^{-5}T^3$	6.62 (300 K)

3 summarizes the host matrix, temperature range, FIR mode, and maximum relative sensitivity (S_r) for these materials. As evidenced by the data, the LiYMoO:Tb^{3+}/Eu^{3+} phosphor investigated in this work exhibits a remarkably high maximum relative sensitivity of 6.5% K^{-1} (300 K). This value significantly exceeds that of many established oxide, fluoride, and phosphate hosts, such as $CaWO_4$ (4.01% K^{-1}) and $LiLaP_4O_{12}$ (1.00% K^{-1}). The superior sensitivity in our system can likely be attributed to the efficient phonon-assisted energy transfer between the Tb^{3+} and Eu^{3+} ions within the molybdate host. This confirms that the prepared material is a top-tier candidate for high-sensitivity optical thermometry applications. The temperature range of 300–403 K was chosen to ensure reliable and reproducible measurements while avoiding potential thermal degradation of the phosphors. Within this range, the FIR exhibits a clear and monotonic increase, allowing accurate evaluation of the temperature sensitivity. At higher temperatures, although the FIR trend suggests that sensitivity may continue to increase, thermal quenching and possible lattice distortions could reduce emission intensity and measurement stability. Therefore, the selected range provides a practical balance between sensitivity and the structural and optical stability of the phosphor material, ensuring accurate temperature sensing while maintaining reproducible luminescence performance.

To evaluate the reliability of the temperature sensing performance, the thermometric parameters (FIR values) were systematically measured over repeated heating–cooling cycles between 300 K and 403 K, as illustrated in Fig. 9. The repeatability (R) of the sensor was calculated using the following expression:[27]

$$R_p(100\%) = 1 - \frac{\max M_i(T)_c \times M(T)_c}{\mathrm{FIR}_c} \times 100 \quad (5)$$

where $M(T)_c$ represents the average FIR value at a given temperature over 10 cycles, and $M_i(T)_c$ corresponds to the FIR value obtained during the ith cycle. The obtained results reveal that the FIR values exhibit reversible and stable behavior throughout the investigated temperature range. The calculated repeatability values for $FIR_1(I_{585}/I_{612})$, $FIR_2(I_{485}/I_{701})$, $FIR_3(I_{542}/I_{612})$ and $FIR_4(I_{542}/I_{701})$ are 97%, 96%, 94%, and 95%, respectively. These results confirm the excellent stability,

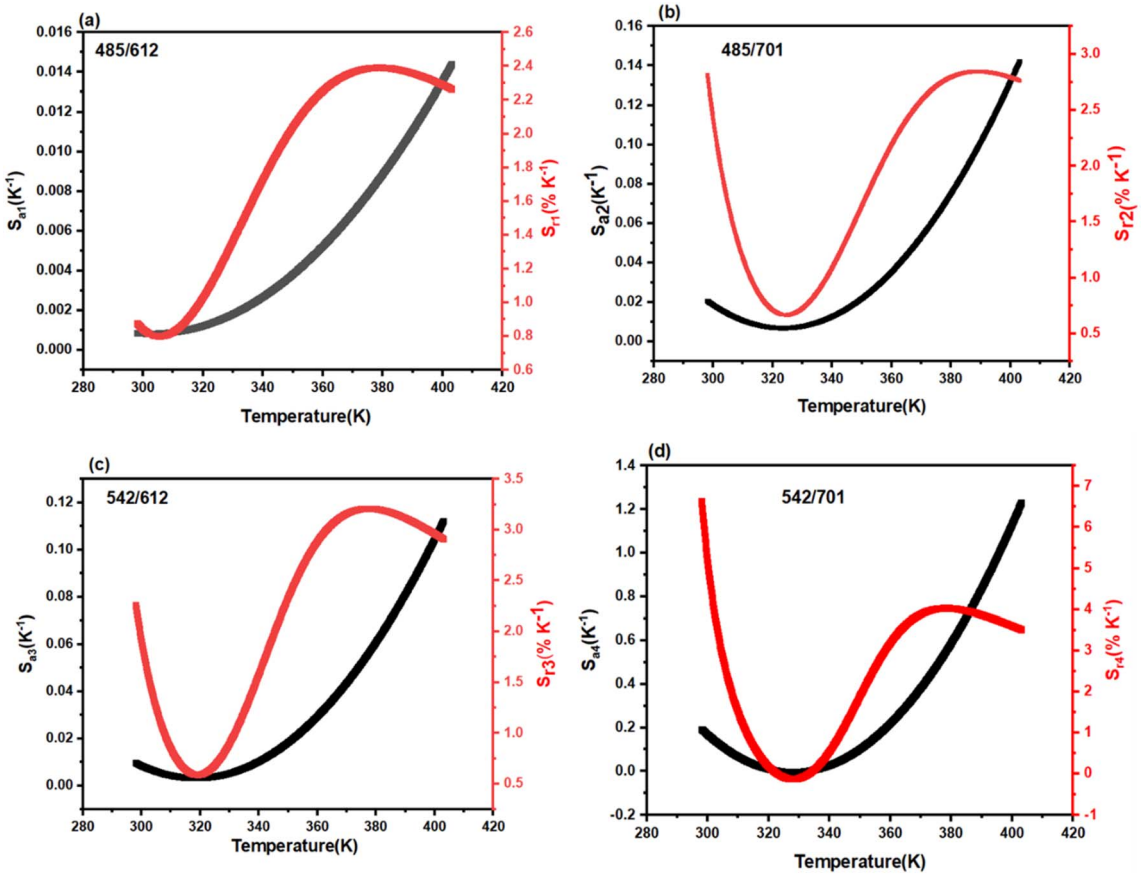

Fig. 8 Temperature dependence of the absolute sensitivity S_a (K^{-1}, left axis) and relative sensitivity S_r (% K^{-1}, right axis) for the co-doped $Li_2Y_4(MoO_4)_7$:Tb^{3+} (40 mol%)/Eu^{3+} (5 mol%) phosphor under 325 nm excitation, calculated from four independent fluorescence intensity ratio (FIR/LIR) combinations: (a) $FIR_1 = I_{485}/I_{612}$, based on the Tb^{3+} $^5D_4 \rightarrow {}^7F_3$ (485 nm) and Eu^{3+} $^5D_0 \rightarrow {}^7F_2$ (612 nm) transitions; (b) $FIR_2 = I_{485}/I_{701}$, based on the Tb^{3+} $^5D_4 \rightarrow {}^7F_3$ (485 nm) and Eu^{3+} $^5D_0 \rightarrow {}^7F_4$ (701 nm) transitions; (c) $FIR_3 = I_{542}/I_{612}$, based on the Tb^{3+} $^5D_4 \rightarrow {}^7F_5$ (542 nm) and Eu^{3+} $^5D_0 \rightarrow {}^7F_2$ (612 nm) transitions; and (d) $FIR_4 = I_{542}/I_{701}$, based on the Tb^{3+} $^5D_4 \rightarrow {}^7F_5$ (542 nm) and Eu^{3+} $^5D_0 \rightarrow {}^7F_4$ (701 nm) transitions, over the temperature range 300–403 K.

Table 3 Comparison of optical thermometric performance (relative sensitivity S_r) of various Tb^{3+}/Eu^{3+} co-doped phosphors reported in the literature

Host matrix	Temp. range (K)	FIR transition pair	Max S_r (% K^{-1})	Ref.
$Li_2Y_4(MoO_4)_7$ (LiYMoO)	300–403	$Tb(^5D_4)/Eu(^5D_0)$	6.5	This work
$CaWO_4$	303–573	$Tb(^5D_4)/Eu(^5D_0)$	4.01	26
$LiLaP_4O_{12}$	303–753	$Tb(^5D_4)/Eu(^5D_0)$	1.00	27
$NaCaPO_4$ (glass ceramic)	298–573	$Tb(^5D_4)/Eu(^5D_0)$	0.66	28
$Sr_8MgLa(PO_4)_7$	298–523	$Tb(^5D_4)/Eu(^5D_0)$	0.16	29
$NaGd(MoO_4)_2$	300–500	$Tb(^5D_4)/Eu(^5D_0)$	1.25	30
Gd_2O_3	303–873	$Tb(^5D_4)/Eu(^5D_0)$	0.82	31

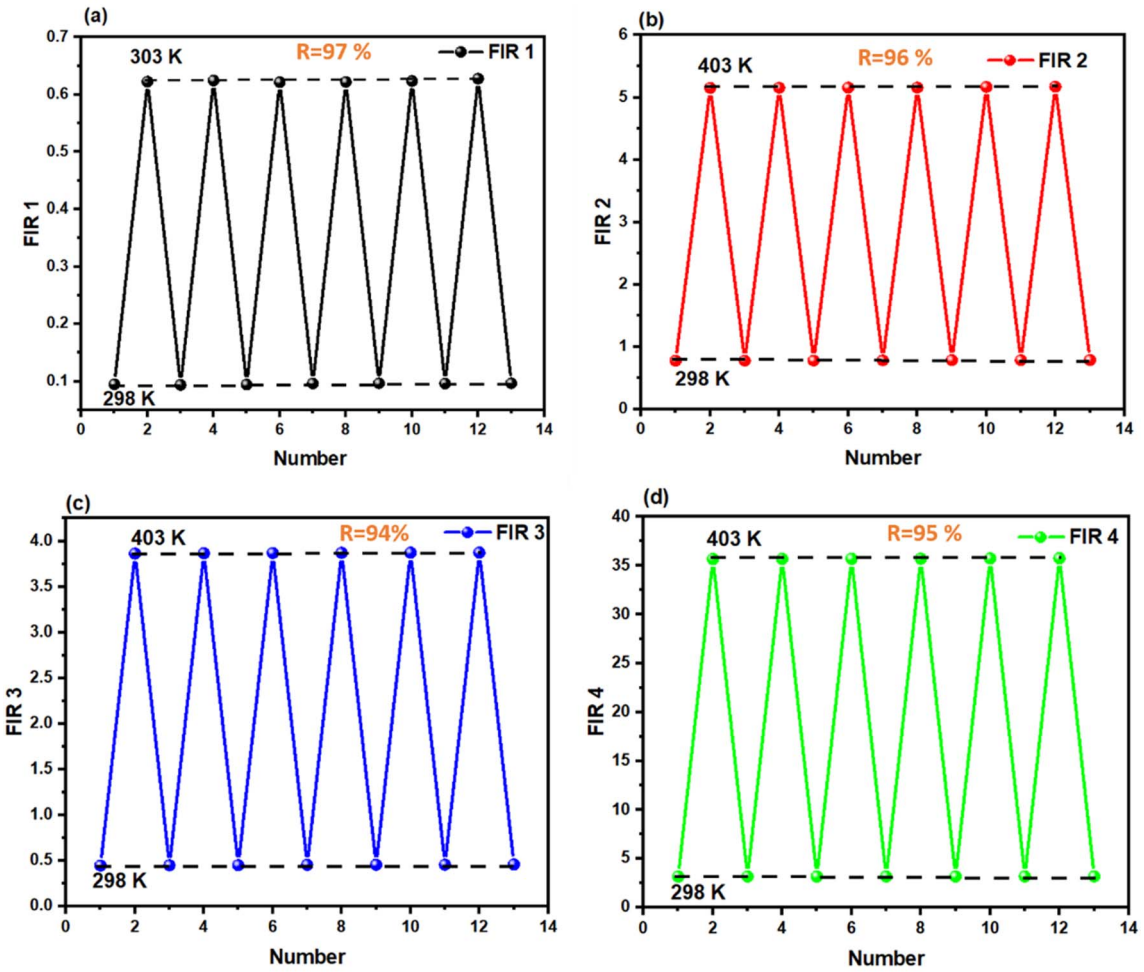

Fig. 9 Repeatability assessment (R) (a) $FIR_1(I_{585}/I_{612})$ (b) $FIR_2(I_{485}/I_{701})$, (c) $FIR_3(I_{542}/I_{612})$ and (d) $FIR_4(I_{542}/I_{701})$ for LiYMoO phosphors.

reliability, and reproducibility of the proposed optical thermometry approach.[32,33]

6. Conclusions

In summary, single-phase $Li_2Y_4(MoO_4)_7$ (LiYMoO) phosphors doped with 40% Tb^{3+}, 5% Eu^{3+}, and co-doped with 40% Tb^{3+}/5% Eu^{3+} were successfully synthesized *via* a high-temperature solid-state reaction method. Structural and morphological characterizations confirmed that the incorporation of activator ions preserved the tetragonal crystal lattice and resulted in uniform microparticles suitable for luminescent applications. Under near-UV excitation (325 nm), the co-doped samples exhibited a tunable dual-emission profile, featuring the characteristic transitions of both Tb^{3+} (green) and Eu^{3+} (red) ions. The spectral evolution provided clear evidence of an efficient Tb^{3+} to Eu^{3+} non-radiative energy transfer mechanism. Crucially, the material demonstrated exceptional performance

as a radiometric optical thermometer. By employing the Fluorescence Intensity Ratio (FIR) technique based on the non-thermally coupled transitions of Tb^{3+} ($^5D_4 \rightarrow {}^7F_5$ at 542 nm) and Eu^{3+} ($^5D_0 \rightarrow {}^7F_4$ at 701 nm), a reliable thermal response was established over the working range of 300–403 K. The sensor achieved a superior maximum relative sensitivity (S_r) of 6.5% K^{-1} at 300 K, significantly outperforming many comparable molybdate and phosphate hosts. These findings position the Tb^{3+}/Eu^{3+} codoped $Li_2Y_4(MoO_4)_7$ system as a highly promising candidate for high-sensitivity contactless temperature sensing devices.

Conflicts of interest

There are no conflicts to declare.

Data availability

All data underlying the results are available as part of the article and no additional source data are required.

References

1 F. Ayachi, K. Saidi, K. Soler-Carracedo, M. Dammak and I. R. Martín, *J. Alloys Compd.*, 2023, **961**, 171146.
2 F. Ayachi, K. Saidi, W. Chaabani and M. Dammak, *J. Lumin.*, 2021, **240**, 118451.
3 B. Koudsi, H. Refai and J. J. Sluss, *J. Disp. Technol.*, 2015, **11**, 266–272.
4 X. Zhang, J. Wang, L. Huang, F. Pan, Y. Chen, B. Lei, M. Peng and M. Wu, *ACS Appl. Mater. Interfaces*, 2015, **7**, 10044–10054.
5 H. M. Yang, J. X. Shi and M. L. Gong, *J. Solid State Chem.*, 2005, **178**, 917–920.
6 E. Castellano-Hernández, X. Han, M. Rico, L. Roso, C. Cascales and C. Zaldo, *Opt. Express*, 2015, **23**, 11135–11140.
7 B. Kukliński, D. Wileńska, S. Mahlik, K. Szczodrowski, M. Grinberg and A. M. Kłonkowski, *Opt. Mater.*, 2014, **36**, 633–638.
8 F. Ayachi, K. Saidi, M. Dammak, I. Mediavilla and J. Jiménez, *RSC Adv.*, 2025, **15**, 655–664.
9 Z. E. A. A. Taleb, I. Kachou, K. Saidi, M. Dammak, I. Mediavilla and J. Jiménez, *Mater. Adv.*, 2025, **6**, 2385–2396.
10 X. Zhang, L. Zhou, J. Shi and M. Gong, *Mater. Lett.*, 2014, **137**, 32–35.
11 Z. Yahiaoui, M. A. Hassairi, M. Dammak, E. Cavalli and F. Mezzadri, *J. Lumin.*, 2018, **194**, 96–101.
12 F. Ayachi, K. Saidi, M. Dammak, J. J. Carvajal and M. C. Pujol, *RSC Adv.*, 2024, **14**, 13494–13504.
13 K. Saidi, M. Dammak, K. Soler-Carracedo and I. R. Martín, *Dalton Trans.*, 2022, **51**, 5108–5117.
14 K. Saidi and M. Dammak, *J. Solid State Chem.*, 2021, **300**, 122214.
15 N. Ben Amar, K. Saidi, C. Hernández-Álvarez, M. Dammak and I. R. Martín, *ACS Appl. Nano Mater.*, 2025, **8**, 17133–17143.
16 I. Kachou, K. Saidi, R. Salhi and M. Dammak, *RSC Adv.*, 2022, **12**, 7529–7539.
17 K. Saidi and M. Dammak, *RSC Adv.*, 2020, **10**, 21867–21875.
18 C. Harriswangler, J. C. Frías, M. T. Albelda, L. Valencia, E. García-España, D. Esteban-Gómez and C. Platas-Iglesias, *Inorg. Chem.*, 2023, **62**, 17030–17040.
19 M. Fan, L. Zhao, X. Jin, W. Sun, W. Qi and Y. Li, *Anal. Chim. Acta*, 2022, **1221**, 340026.
20 B. Wang, Q. Ren, O. Hai and X. Wu, *RSC Adv.*, 2017, **7**, 15222–15227.
21 Q. Han, H. Hao, J. Yang, Z. Sun, J. Sun, Y. Song, Y. Wang and X. Zhang, *J. Alloys Compd.*, 2019, **786**, 770–778.
22 S. Bhushan and M. V. Chukichev, *J. Mater. Sci. Lett.*, 1988, **7**, 319–321.
23 Y. Bahrouni, I. Kachou, K. Saidi, C. Hernández-Álvarez, M. Dammak and I. R. Martín, *RSC Adv.*, 2026, **16**, 4452–4460.
24 M. Fhoula, M. Khitouni and M. Dammak, *RSC Adv.*, 2024, **14**, 39373–39380.
25 Y. Jiang, Y. Tong, S. Chen, W. Zhang, F. Hu, R. Wei and H. Guo, *Chem. Eng. J.*, 2021, **413**, 127470.
26 M. D. Dramićanin, *J. Appl. Phys.*, 2020, **128**, 040902.
27 Y. Bahrouni, I. Kachou, K. Saidi, C. Hernández-Álvarez, M. Dammak and I. R. Martín, *J. Alloys Compd.*, 2026, **1056**, 186657.
28 Y. Zhang, W. Gong, J. Yu, Z. Cheng and G. Ning, *RSC Adv.*, 2016, **6**, 30886–30894.
29 L. Marciniak and A. Bednarkiewicz, *Phys. Chem. Chem. Phys.*, 2016, **18**, 15584–15592.
30 L.-Q. Yao, G.-H. Chen, T. Yang, S.-C. Cui, Z.-C. Li and Y. Yang, *Ceram. Int.*, 2016, **42**, 13086–13090.
31 W. Xia, L. Li, P. Yang, F. Ling, Y. Wang, Z. Cao, S. Jiang, G. Xiang, X. Zhou and Y. Hua, *J. Lumin.*, 2021, **239**, 118383.
32 L. Peng, Q. Meng and W. Sun, *Ceram. Int.*, 2019, **45**, 20656–20663.
33 I. E. Kolesnikov, D. V. Mamonova, M. A. Kurochkin, V. A. Medvedev, E. V. Borisov and E. Y. Kolesnikov, *Ceram. Int.*, 2023, **49**, 6899–6905.